# Solution Processable High Dielectric Constant Nanocomposites Based on ZrO$_2$ Nanoparticles for Flexible Organic Transistors

Michael R. Beaulieu,[†] Jayanta K. Baral,[†] Nicholas R. Hendricks, YuYing Tang, Alejandro L. Briseño,* and James J. Watkins*

Department of Polymer Science and Engineering, University of Massachusetts Amherst, 120 Governors Drive, Amherst, Massachusetts 01003, United States

ABSTRACT: A solution-based strategy for fabrication of high dielectric constant (κ) nanocomposites for flexible organic field effect transistors (OFETs) has been developed. The nanocomposite was composed of a high-κ polymer, cyanoethyl pullulan (CYELP), and a high-κ nanoparticle, zirconium dioxide (ZrO$_2$). Organic field effect transistors (OFETs) based on neat CYELP exhibited anomalous behavior during device operation, such as large hysteresis and variable threshold voltages, which yielded inconsistent devices and poor electrical characteristics. To improve the stability of the OFET, we introduced ZrO$_2$ nanoparticles that bind with residual functional groups on the high-κ polymer, which reduces the number of charge trapping sites. The nanoparticles, which serve as physical cross-links, reduce the hysteresis without decreasing the dielectric constant. The dielectric constant of the nanocomposites was tuned over the range of 15.6−21 by varying the ratio of the two components in the composite dielectrics, resulting in a high areal capacitance between 51 and 74 nF cm^{-2} at 100 kHz and good insulating properties of a low leakage current of 1.8×10^{-6} A cm^{-2} at an applied voltage of −3.5 V (0.25 MV cm^{-1}). Bottom-gate, top-contact (BGTC) low operating voltage p-channel OFETs using these solution processable high-κ nanocomposites were fabricated by a contact film transfer (CFT) technique with poly(3-hexylthiophene) (P3HT) as the charge transport layer. Field effect mobilities as high as 0.08 cm^2 V^{-1} s^{-1} and on/off current ratio of 1.2×10^3 for P3HT were measured for devices using the high-κ dielectric ZrO$_2$ nanocomposite. These materials are promising for generating solution coatable dielectrics for low cost, large area, low operating voltage flexible transistors.

KEYWORDS: zirconium dioxide, high dielectric constant (κ), nanocomposite, low voltage organic thin film transistor
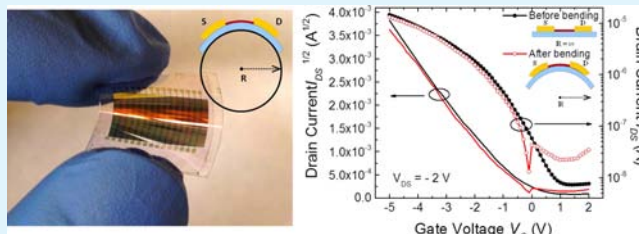
INTRODUCTION

Organic field effect transistors (OFETs) have garnered significant interest for use in low cost, lightweight, and flexible electronics.[1−4] Much of the research effort within the field of flexible OFETs has focused on the mobility of the semiconductor. However, a great deal of effort is being directed toward generating improved gate dielectrics[5,6] for low voltage alternatives to silicon-based technologies. Reduced operation voltages can be realized through the use of high dielectric constant (κ) metal oxide films.[2] Typically, high-κ metal oxide films are deposited by either sputtering[7] or anodization.[5] Both of these methods have drawbacks; sputtering is prohibitively expensive, and anodization limits patterning options, since many metal oxides are etch resistant to standard etchants. Another limitation to sputtering or anodization is the poor mechanical properties of the resulting metal oxide thin films. Since this area of research has produced a large quantity of publications, it is not possible to examine all the interesting contributions in high-κ dielectrics from physical deposition or high temperature sintering methods, at least within the scope of this paper, there are many review papers that discuss these methods.[2,8] A low cost alternative process for high-κ dielectrics is desirable for large area flexible electronics. One strategy is to generate high-κ polymer nanocomposites using solution-based methods.

Spin-coating, gravure, and Mayer rod coating are common methods for the fabrication of thin polymer films (10−1000 nm). Most common polymers have relatively low dielectric constants ($\kappa \approx 2-4$);[8,9] thus, very thin layers are required to generate high capacitance. Coating of thin polymeric films with thicknesses less than 10 nm often results in structural heterogeneities, such as pinholes, leading to large gate leakages.[10,11] Defect-free thin polymeric films have been generated, by using cross-linking agents to produce low voltage and, more importantly, low leakage current thin-film transistors (TFTs).[10,12−14] However, the cross-linking chemistries used are typically water and/or air sensitive and thus unsuited for coating at ambient conditions.

An alternative method to generate high capacitance dielectric layers is to increase the dielectric constant of the film by incorporating high-κ metal oxide nanoparticles into polymers to form polymer nanocomposites.[15−21] Both in situ[22] and ex situ
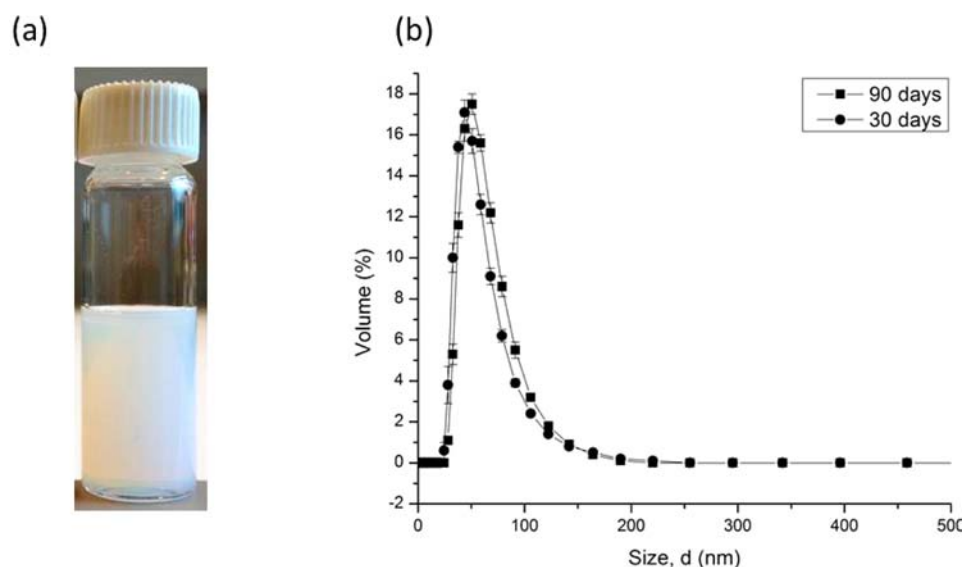
Figure 1. (a) Optical image of an 8 wt % ZrO_2 nanoparticles dispersion in a solution composed of equal parts NMP and MeOH. (b) Particle size distributions of 8 wt % ZrO_2 nanoparticle dispersions after 30 days (circles) and 90 days (squares) were measured using a Malvern Zetasizer.

strategies are used to generate high-κ metal oxides within a polymeric host.[15,19,23] In situ generation of metal oxides within a polymer is achieved using sol−gel chemistries followed by post processing, including thermal, chemical, electrochemical, or photoirradiation treatments.[24] These post processing steps can be detrimental to the polymer binder phase of the composite or to the flexible substrate. To avoid the harsh conditions associated with in−situ generated nanocomposites, ex situ methods have been utilized.

Ex situ nanoparticle synthesis separates the nanocomposite formation from the nanoparticle generation. This is advantageous as processing steps, such as thermal, hydrothermal, or ultraviolet (UV) light used to create the desired crystalline phase or surface functionality, are conducted prior to nanocomposite formation without degrading the polymer binder or flexible substrate. Ex situ nanoparticle generation has shown promise for many applications including solar cells,[25] supercapacitors,[26] sensors,[27] batteries,[28] and nanocomposite based dielectrics.[16,19] In one example, titanium dioxide (TiO_2) nanoparticles with polystyrene ligands were used to create a solution processable high-κ layer for OFETs. However, the dielectric constant was only modestly improved to 5.3 and the synthesis strategy was labor intensive.[16] Other strategies to develop solution processable high-κ dielectric layers for OFETs have been developed using a number of different metal oxides, such as TiO_2, barium titanate ($BaTiO_3$), strontium titanate ($SrTiO_3$), and aluminum oxide (Al_2O_3).[2] A new strategy for low operating voltage OFETs using solution-processable high-κ amorphous oxides as gate dielectrics has been recently reported.[29−31] The metal oxide layers are generated by coating a sol−gel precursor and subsequent densification. The densification method can be achieved using high intensity UV sources, which generates a thin amorphous film. However, the authors have not discussed the hysteresis effects in their OFETs using the solution-processable metal oxides as gate dielectrics, since the hysteresis effects in OFETs have been an ongoing topic of discussion for its limitations to the commercial viability in the field of flexible displays. In this work, we report the first high-κ nanocomposite based on commercially available nanoparticles, zirconium dioxide

(ZrO_2), for use in low voltage OFETs. The influence of ZrO_2 nanoparticle loading on the hysteresis, dielectric constant, leakage current, dielectric breakdown, and mobility was evaluated and discussed. The optimal composition of the ZrO_2 nanocomposite was identified to generate low hysteresis OFETs.

■ EXPERIMENTAL SECTION

Materials. Zirconium dioxide nanoparticle (50 nm average particle size) dispersions in water (14 wt %, Nyacol Nano Technologies, Inc.), cyanoethyl pullulan (CYELP, Shin-Etsu Chemical Company, Ltd.), N-methyl pyrrolidone (NMP, Reagent Plus 99% Sigma-Aldrich), methanol (MeOH, ACS grade, Fisher Scientific), isopropanol (ACS grade, Fisher Scientific), chlorobenzene (ACS grade, Sigma-Aldrich), n-octadecyl phosphonic acid (ODPA, 97%, Sigma-Aldrich), sodium poly(styrene sulfonate) (Sigma-Aldrich), poly(3-hexylthiophene) (P3HT) (M_w = 50 kg/mol, Rieke Metals, Inc.), and poly(ethylene naphthalate) substrates (PEN, 125 μm planarized Teonex) were used as received. Low resistivity silicon wafers ((100) orientation, p-type, boron dopant) were obtained from University Wafer.

Solvent Exchange of Zirconium Dioxide Nanoparticles. A 250 mL Pyrex screw cap bottle was charged with 100 g of the ZrO_2 water based dispersion. To this dispersion, 100 g of equal amounts (by weight) of MeOH and NMP were added and mixed. This solution was dried slowly with a constant flow of air for extended periods of time, until the majority of the solvent was removed (greater than 50%). This dried nanoparticle slurry was then redispersed with the desired mixture of MeOH and NMP through sonication and mixing. The resulting dispersions had a nanoparticle concentration greater than 15 wt %. These organic solvent-based nanoparticle dispersions were stable for several months. Particle size and particle size distributions (PSDs) were measured by using a Malvern Zetasizer 3000 HAS (Malvern Instruments Ltd., Malvern, U.K.) at a temperature of 25 °C and a scattering angle of 90° after diluting the nanoparticle suspension to 5 wt % solids. The PSD was based on five different measurements.

Thin Film Transistor Preparation and Characterization. The transistors were fabricated on PEN substrates by first thermally evaporating 20 nm of aluminum (Al) prior to spin-coating the ZrO_2 nanocomposite layer. CYELP was dissolved in NMP to create a 15 wt % solution. The solvent exchanged nanoparticles were added to the CYELP solution to obtain the desired composition. Once the composition was generated, the ZrO_2/CYELP nanocomposite was sonicated for 15 min and spin-coated on the Al coated PEN at 3000 rpm. The film thickness ranged from 250 to 265 nm, as measured by
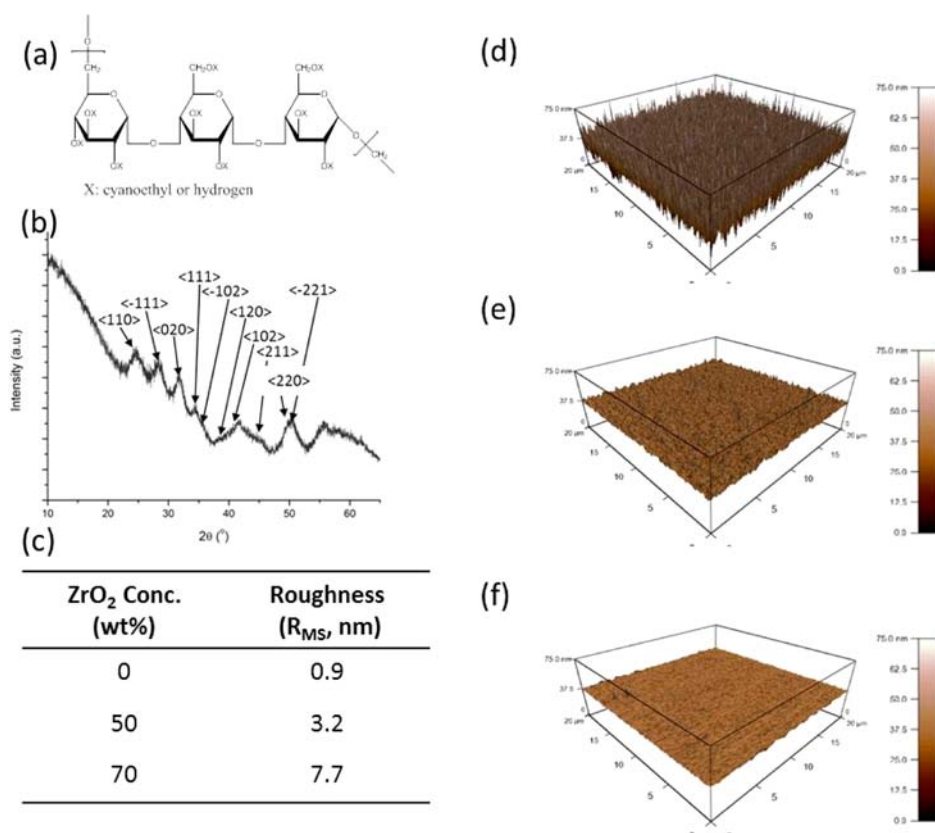
Figure 2. (a) Chemical structure of CYELP. (b) XRD of the ZrO_2 nanoparticle powder, showing a monoclinic crystalline phase. (c) RMS roughness values of several compositions based on 20 μm × 20 μm AFM scans, with the corresponding 3D height images for (d) 90 wt % ZrO_2 nanoparticles and 10 wt % CYELP, (e) 50 wt % ZrO_2 nanoparticles and 50 wt % CYELP, and (f) 0 wt % ZrO_2 nanoparticles and 100 wt % CYELP.

interferometry. Passivation of the ZrO_2/CYELP layer was carried out by immersing the dielectric coated PEN layer in a 5×10^{-3} M ODPA in 2-propanol overnight. The excess ODPA was removed by sonication in pure 2-propanol and dried under a stream of nitrogen (N_2). The semiconductor layer was deposited by a contact film transfer (CFT) printing method that has been previously reported.[32−34] Briefly, a water-soluble, release layer, sodium poly-(styrene sulfonate) (PSS), was spin-coated on a glass slide that was previously cleaned with sulfuric acid. Next, a P3HT solution in chlorobenzene (2 mg/mL) was successively spin-coated on top of the PSS layer to generate a film with the structure of glass/PSS/P3HT. This film was then brought into contact with the surface passivated ZrO_2 nanocomposite layer. A single drop of water was placed at the edge of these substrates, and the water dissolved the PSS layer, detaching the P3HT from the upper substrate. Gold electrodes were then deposited on top of the P3HT by thermal evaporation through a shadow mask of channel length, $L = 100$ μm, and channel width, $W = 3$ mm, to complete the fabrication of the p-channel OFET. The electrical characteristics of the bottom-gate top-contact (BGTC) P3HT based p-channel OFETs were measured under vacuum (~1 × 10^{-4} Torr) using a Keithley 2400 SCS unit at room temperature. The capacitance (C) for each of the nanocomposite compositions was measured by placing the dielectric layer between highly doped p-type (100) silicon substrates with a Keithley 4200 semiconductor characterization system using a Wentworth MP-2300 probe station at 100 kHz. All device measurements were performed in the dark. X-ray diffraction (XRD) experiments were conducted on a PANalytical X'Pert diffractometer, using copper (Cu) Kα X-rays (0.1542 nm) operating at 45 kV and 40 mA. The root-mean-square roughness (RMS) was measured over 20 μm × 20 μm scans using an Asylum MFP3D atomic force microscope (AFM).

RESULTS AND DISCUSSION

The ZrO_2 nanoparticle dispersion was obtained from Nyacol Nano Technologies, Inc. as a nitrate stabilized water dispersion with a particle diameter of 50 nm. The ZrO_2 nanoparticle dispersion was solvent−exchanged from water to a mixture of polar solvents. This exchange was necessary to dissolve the high-κ polymer, cyanoethyl pullulan (CYELP), to generate stable dispersions for solution coatable dielectrics (Figure 1a). The degree of cyanoethylation was greater than 90% and the structure of the CYELP polymer is shown in Figure 2a.[35] The solvent system that proved to be most useful for generating uniform dielectric films was equal parts by weight of N-methyl pyrrolidone (NMP) and methanol (MeOH). The solvent exchanged ZrO_2 nanoparticle dispersions were very stable, since the particle size distribution did not change over the course of several months, Figure 1b. These ex situ synthesized ZrO_2 nanoparticles were characterized by X-ray diffraction (Figure 2b) and exhibited a monoclinic crystalline phase. The roughness of the ZrO_2 nanocomposite was characterized using atomic force microscopy (AFM) (Figure 2c). The corresponding 3D height images for the different compositions are shown in Figure 2d−f. The films were spin-coated from 11−13 wt % solutions at 3000 rpm to generate uniform films, with thicknesses ranging from 250 to 265 nm. The root-mean-squared (RMS) roughness of the films ranged from 7.7 to 0.9 nm for 70 and 0 wt % ZrO_2 nanoparticles, respectively.

From a capacitor of metal−insulator−semiconductor (MIS) structure, shown in Figure 3a, the dielectric constant of the ZrO_2 nanocomposite was measured using eq 1, where C_{ox} is the areal capacitance of the gate (dielectric) oxide, ε (relative static
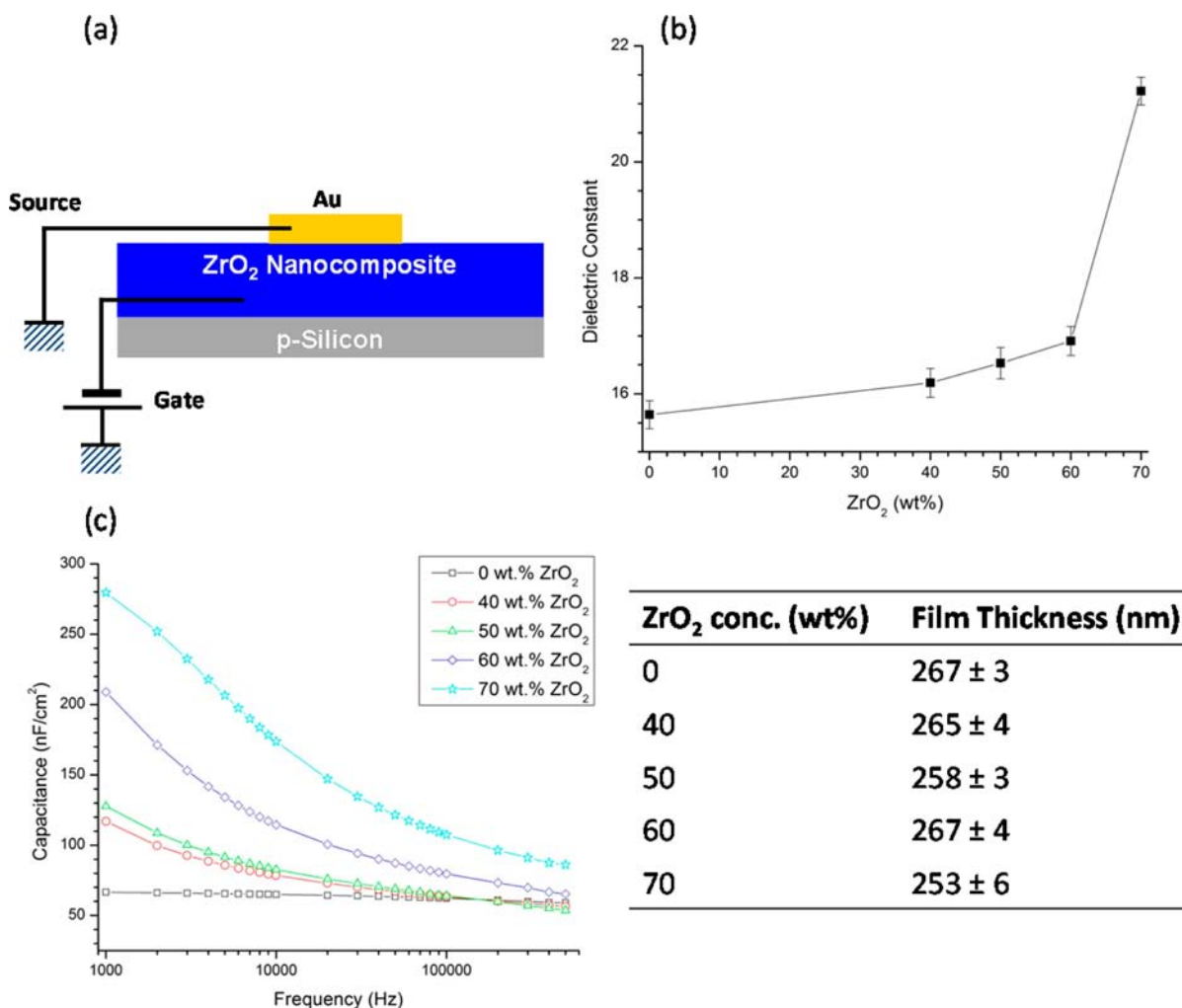
Figure 3. (a) Schematic of the MIS device probed to measure the capacitance of the ZrO$_2$ nanocomposites. (b) Dielectric constant calculated from the capacitance measurement versus the concentration of ZrO$_2$ nanoparticles at a frequency of 100 kHz. (c) Capacitance versus frequency for the different ZrO$_2$ nanocomposites used in this study. (d) Film thicknesses of the ZrO$_2$ nanocomposites which were used to calculate capacitance and dielectric constant.

permittivity) $= \kappa$ (dielectric constant) $\times \varepsilon_0$ (electric constant $\approx$ 8.854 $\times$ 10^{-12} F m^{-1}), A is the area of overlap between the parallel plate capacitors, and d is the thickness of the dielectric layer. The dielectric constant for pure crystalline ZrO$_2$ ranges between 18 and 35 based on the particle size, crystal morphology, and degree of crystallinity of the ZrO$_2$.[36] When the ZrO$_2$ nanoparticles were blended with the CYELP polymer, the dielectric constant was increased from 15.6 to 21.22 for 0 wt % ZrO$_2$ and 70 wt % ZrO$_2$ respectively, Figure 3b. The areal capacitance values for 0 wt % ZrO$_2$ and 70 wt % ZrO$_2$ resulted in capacitance values of 50 and 75 nF cm^{-2}, respectively (film thicknesses used for the calculation of capacitance can be seen in Figure 3d).

$$C_{ox} = \frac{\varepsilon A}{d} = \frac{k\varepsilon_0 A}{d} \qquad (1)$$

Figure 4a shows the schematic representation of BGTC P3HT based OFETs. To increase the compatibility between the nanocomposites with the relatively nonpolar P3HT semiconductor, the composite surface was modified using ODPA. The ODPA is capable of reacting with the remaining hydroxyl groups from the CYELP polymer, as well as the native oxide surfaces of the ZrO$_2$ nanoparticles. After treating the

dielectric layer with the ODPA to form a self-assembled monolayer (SAM), the P3HT layer was deposited on top through a contact film transfer technique (CFT).[33] It has been observed that P3HT films deposited using CFT have higher mobilities, than that of the spin-coated thin films, due to increased molecular orientation and interchain $\pi-\pi$ inter-actions, and these mechanisms are in good agreement with our previous findings.[33] The CFT method relies on differential adhesion for the transfer of a printable layer from the transfer substrate to the device substrate. In this transfer-printing technique, a water-soluble polymer, sodium poly(styrene sulfonate) (PSS) was used as a sacrificial layer. The transfer substrate, glass, was coated by successively spin coating an aqueous solution of PSS and a chlorobenzene solution of P3HT. Inverting the transfer substrate, so the P3HT film was in contact with the ODPA coated ZrO$_2$ nanocomposite allowed for the P3HT to be transferred onto the dielectric by dissolving the sacrificial layer in water. The glass substrate was then easily detached from the polymer surface. Gold electrodes were then deposited on top of the P3HT by thermal evaporation through a shadow mask of $L = 100$ μm and $W = 3$ mm, to complete the fabrication of the BGTC OFET. Figure 4b shows the transfer curve of a typical OFET based on the neat CYELP polymer as
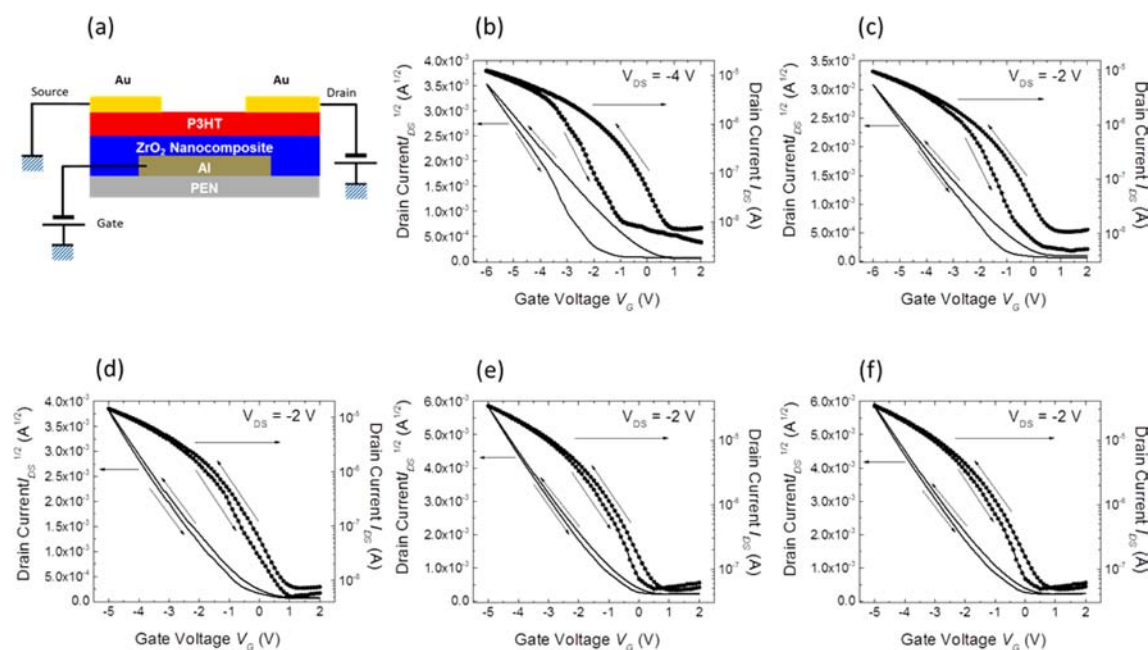
Figure 4. (a) Illustration of the OFET geometry used for this work. The OFET is a bottom-gate top-contact transistor with a solution coatable ZrO_2 nanocomposite dielectric layer. Transfer curves of the resulting OFETs coated with different concentrations of ZrO_2 nanoparticle and CYELP, (b) 0 wt % ZrO_2 and 100 wt % CYELP, (c) 40 wt % ZrO_2 and 60 wt % CYELP, (d) 50 wt % ZrO_2 and 50 wt % CYELP, (e) 60 wt % ZrO_2 and 40 wt % CYELP, and (f) 70 wt % ZrO_2 and 30 wt % CYELP.

Table 1. Transistor Characteristics with ZrO_2 Nanocomposite Dielectrics at Different Nanoparticle Loadings

ZrO_2 conc. (wt %)	V_{th} (V)	ΔV_{th} shift (V)	ON/OFF current ratio ($\times 10^3$)	mobility, μ ($\times 10^{-2}$ cm^2/V·s)	leakage current ($\times 10^{-6}$ A/cm^2) at -3.5 V	dielectric breakdown strength (MV/cm)
0	-1.8 ± 0.3	1.2 ± 0.2	1.3 ± 0.1	4.2 ± 2.4	1.1 ± 0.3	0.30 ± 0.12
40	-1.2 ± 0.2	0.4 ± 0.2	1.1 ± 0.2	7.0 ± 1.2	1.4 ± 0.4	0.27 ± 0.1
50	-1.0 ± 0.2	0.2 ± 0.1	1.2 ± 0.1	8.0 ± 1.2	1.8 ± 0.3	0.27 ± 0.08
60	-1.0 ± 0.2	0.2 ± 0.1	0.6 ± 0.1	6.0 ± 1.4	1.5 ± 0.4	0.28 ± 0.12
70	-1.0 ± 0.2	0.2 ± 0.1	0.6 ± 0.2	5.6 ± 1.2	1.7 ± 0.5	0.27 ± 0.08

the dielectric layer. Using the polymer only dielectric layer causes a large degree of hysteresis with a shift in threshold voltage (ΔV_{th}) of 1.2 ± 0.2 V, whereas, the device turn on/threshold voltage (V_{th}) occurred at -1.8 ± 0.3 V. The field effect hole mobilities (μ_{sat}), of the polymer-only OFETs, were calculated from the saturation regime of the square root of the drain current (I_{DS}) and have been listed in Table 1. The large variation in μ_{sat} has been attributed to the drain current (I_{DS}) hysteresis, while sweeping the gate voltage bias of the OFETs. This phenomenon can presumably be attributed to two mechanisms: (1) long-lived charge traps at the semiconductor/dielectric interface due to defects in the semiconductor film, surface functionalities of the dielectric layer, and absorbed species at the interface (anticlockwise loop hysteresis);[37−42] or (2) slow polarization of polar moieties of the dielectric layer (clockwise loop hysteresis).[40,43−47] This hysteresis leads to a shift in ΔV_{th}, which prevents the use of these dielectric layers in OFETs for applications that require the V_{th} to be stable, such as in driving units used for displays. One strategy that has been utilized to generate hysteresis free high-κ dielectric layers is to covalently cross-link these cyanoethylated polymers, which consumes these excess polar moieties. There are three drawbacks to this technique in terms of scalability or performance: first, the temperature required to cross-link these materials is in excess of 100 °C; second, the time required to fully cross-link the system is longer than 1 h; and

third, the dielectric constant is reduced due to the addition of the polymeric or oligomeric reactive diluent that participates in the cross-linking.[48−50] These drawbacks create limitations to generating OFETs when low cost, large scale, and flexible electronics are the ultimate goal.

Next, nanocomposites were generated and compared to the neat CYELP polymer dielectric OFET. OFETs fabricated using the high-κ dielectric layer with 40 wt % ZrO_2 loadings, exhibited a reduction in the I_{DS} hysteresis as shown in Figure 4c. This improved the V_{th}, which occurred at -1.2 ± 0.2 V and a reduction in the ΔV_{th} 0.4 ± 0.2 V was also observed, when compared to the neat CYELP devices. However, the hysteresis was not completely suppressed as can be seen in Figure 4c. An enhanced μ_{sat} of 0.07 ± 0.012 cm^2/V·s was also observed from these 40 wt % ZrO_2 devices as compared to the large variation in μ_{sat} from the neat CYELP devices. As the concentrations of ZrO_2 nanoparticles were further increased above 40 wt %, the hysteresis was further suppressed as shown in Figure 4d−f. OFETs with dielectric layers that were composed of 50, 60, or 70 wt % ZrO_2 nanoparticles, respectively, exhibited consistent device operation at low V_{th}, -1.0 ± 0.2 V, and a significant reduction in ΔV_{th}, 0.2 ± 0.1 V. Again, the hysteresis was not completely removed; however, the OFETs fabricated with ZrO_2 nanoparticles as gate dielectrics have exhibited improved transistor characteristics as compared to the polymer only device, listed in Table 1. The physical cross-links imparted by

the ZrO_2 nanoparticles with the CYELP polymer are sufficient to reduce the hysteresis, without a reduction in the dielectric constant, and do not require a high temperature annealing step. This reduction in hysteresis is mainly attributed to the residual hydroxyl (−OH) groups favorably interacting with the metal oxide surface, reducing the concentration of these groups at the $P3HT/ZrO_2$ nanocomposite interface, thereby effectively reducing the I_{DS} hysteresis. It is well-known that the presence of traps, attributed to residual hydroxyl groups at the gate-dielectric/semiconductor interface, significantly contributes to the hysteresis effects.[51] The polymer/nanoparticle nanocomposites reduce the residual −OH groups in the bulk dielectric layer and additionally reduce the number of trap states at the gate-dielectric/semiconductor interface upon nanoparticle loading. Therefore, we have obtained significantly decreased ΔV_{th}; however, the hysteresis effects were not completely suppressed.

Table 1 shows the key parameters evaluated for the electrical characterization from more than 10 samples fabricated with the high-κ dielectrics with different concentrations of ZrO_2 nanoparticles with a CYELP polymer matrix. In Table 1, an increase in field effect hole mobilities (μ_{sat}) has been observed for the OFETs with dielectric layers containing ZrO_2 nanoparticles. Moreover, the physical cross-links between the CYELP and the ZrO_2 nanoparticles reduced the charge traps inside the dielectric layer and on the surface of the gate insulator (i.e., at the insulator/semiconductor interface), producing the lowest ΔV_{th} shift and lower/sharper subthreshold voltage (S).[48] The significant improvements in the μ_{sat} for these p-channel OFETs, subthreshold swing (S), V_{th}, and reduced ΔV_{th} measured can be effectively attributed to the decrease in the charge trap state density at the semiconductor/dielectric interface.[52]

Trapped State Density Estimation. The areal densities of the interfacial traps were estimated by using eq 2,[44,48] where q is the electronic charge, S is the (reciprocal) subthreshold slope (V/decade), k is Boltzmann's constant, T is temperature (K), and C_{ox} is the areal capacitance of the gate (dielectric) oxide. The subthreshold slopes (S) were calculated from the relation, $S = dV_{GS}/d(\log I_{DS})$. The polymer only OFET had an interfacial trap density of 9.2×10^{11} cm^{-2}, whereas the OFETs fabricated from the ZrO_2 nanocomposites exhibited a decrease in interfacial trap states as listed in Table 2. The

Table 2. Trap State Density Estimation of the Various Gate Insulators

ZrO_2 conc. (wt %)	trap states/cm^2
0	9.2×10^{11}
40	5.1×10^{11}
50	4.7×10^{11}
60	5.4×10^{11}
70	5.6×10^{11}

increase in μ_{sat} of the devices based on ZrO_2 nanocomposites, when compared to the polymer dielectric only device, can be ascribed to the elimination of areal trap states inside the dielectric layer and on the surface of the gate insulator (i.e., at the insulator/semiconductor interface).[48] The elimination of trap states lowered the ΔV_{th} shift and reduced the change in subthreshold swing from 0.8 to 0.3 V/decade for the polymer only OFET versus 50 wt % ZrO_2 nanocomposite based OFETs, respectively. It is well-known that a high subthreshold swing is a

drawback of OFETs, resulting from the combination of low gate-dielectric capacitance at the metal/insulator and insulator/semiconductor interfaces.[48] The OFET parameters, listed in Tables 1 and 2, further elucidate the origins of the ΔV_{th} and show that physical cross-linking with ZrO_2 nanoparticles was able to enhance or maintain the properties of the neat CYELP polymer.

$$N_{trap}^{max} \approx \left[\frac{qS \log(e)}{kT} - 1 \right] \frac{C_{ox}}{q} \tag{2}$$

The incorporation of the higher loadings of ZrO_2 nanoparticles does adversely affect two properties. First, the leakage current was slightly increased from $1.1 \pm 0.3 \times 10^{-6}$ A cm^{-2} for the neat CYELP polymer to $1.7 \pm 0.5 \times 10^{-6}$ A cm^{-2} for 70 wt % ZrO_2 nanoparticle based nanocomposite, Figure 5a. The minor increase in leakage current could effectively be attributed to the relative increase in roughness of the nanocomposite films compared to the polymer only dielectric layer. The second property was a reduction in the dielectric breakdown strength, Figure 5b. The breakdown strength decreases from 0.3 MV/cm, for the neat CYELP polymer to 0.27 MV/cm for a concentration of 70 wt % ZrO_2 nanoparticles in the nanocomposites, Table 1. The slight detriments to both the leakage current and the breakdown strength was of minor consequence, when comparing to the large gains in terms of μ_{sat}, V_{th}, and ΔV_{th} shift. The device that had the best performance in terms of all the properties mentioned was 50 wt % ZrO_2 and 50 wt % CYELP, which had the highest μ_{sat} and I_{On}/I_{Off}, as well as lowest V_{th} and ΔV_{th} shift. This particular composition will be the focus of future research involving high throughput manufacturing techniques of OFETs.

To demonstrate the performance and durability of our devices on plastic substrates, we carried out measurements under flexible operating conditions. Our best performing device, that is, fabricated from 50 wt % ZrO_2 and 50 wt % CYELP nanocomposite dielectrics, was chosen to determining the effect of strain on mobility. The digital photograph of a flexible OFET is shown in Figure 6a. Figure 6b shows the transfer curve of the OFET before and after bending five times. Force bending was applied across the source-drain channel of the flexible device to determine the performance characteristics. The strain (ε) produced across the channel of the transistor was calculated from the following expression.[53−56]

$$\varepsilon = \left(\frac{d_f + d_s}{2R} \right) \frac{(1 + 2\eta + \chi\eta^2)}{(1 + \eta +)(1 + \chi\eta)} \approx \frac{d_s}{2R} \tag{3}$$

where ε is the strain, R is the bending radius of curvature, $\chi = Y_f/Y_s$ (Y_f and Y_s are the Young's moduli of the gate dielectric layer and substrate, respectively), and $\eta = d_f/d_s$ (d_f and d_s are the thickness of the gate dielectric layer and substrate, respectively). The thicknesses of the PEN substrate and the gate dielectric layer are approximately 125 μm and 300 nm, respectively. Due to the large difference in thicknesses of the PEN substrate and the gate dielectric layer, the strain can be approximated to be $d_s/2R$. Devices were first characterized in a planar geometry (with 0% strain, i.e., when $R = \infty$) followed by bending the flexible OFET structure around a glass vial at a certain radius of curvature ($R = 0.75$ cm). From this flexibility study, the key transistor parameters characterized from this particular flexible device are tabulated in Table 3. It is noteworthy that the V_{th} and μ_{sat} of the device before and after bending have not changed significantly. However, the
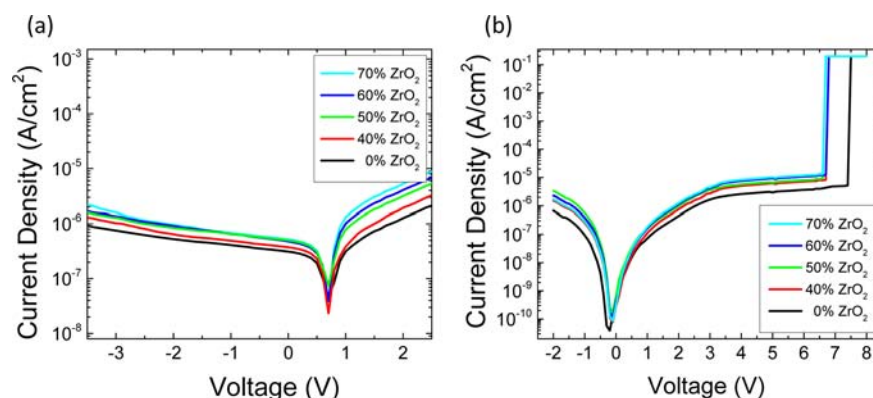
13101

dx.doi.org/10.1021/am404129u | ACS Appl. Mater. Interfaces 2013, 5, 13096−13103

Figure 5. (a) Leakage current measurements as a function of ZrO_2 nanoparticle loadings and (b) dielectric breakdown of the ZrO_2 nanocomposite as a function of ZrO_2 nanoparticle loading.
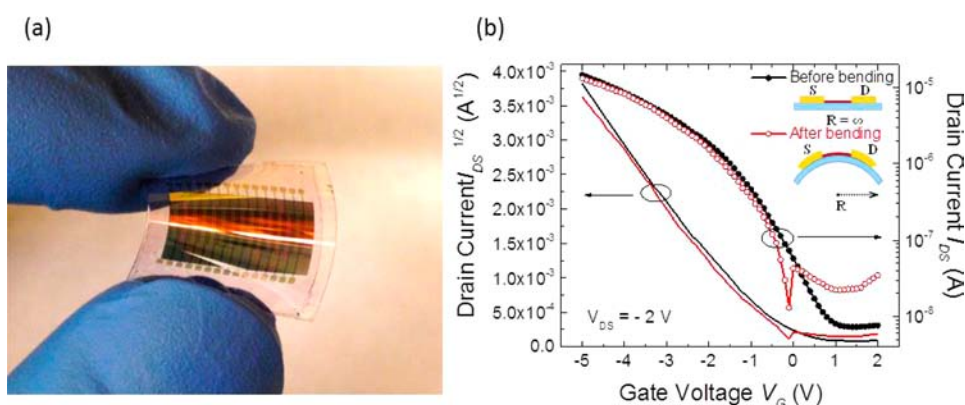

Figure 6. (a) Digital photograph of the fabricated flexible high-κ OFET. All bending measurements were performed on substrates bent across the source-drain channel length. (b) Overlaying the transfer curves characterized before and after flexing the fabricated flexible OFET, measured at $V_{DS} = -2.0$ V. Inset: Schematic illustrations represent the planar and bent OFET structures with their respective bending radii of curvatures.

Table 3. Summary of the Electrical Characteristics of ZrO_2 Dielectric Based High-κ Flexible OFETs before and after Flexing

device	V_{th} (V)	ON/OFF current ratio	mobility, μ (cm^2/V·s)
nonflex OFET	−0.8	2.3×10^3	0.084
flex OFET	−1.0	1.1×10^3	0.078

ON/OFF current ratio changed noticeably upon bending the device to strain of 0.835%. Nevertheless, the performance returned upon measuring the device in its planar (i.e., 0% strain when $R = \infty$) unstrained geometry.

CONCLUSION

In conclusion, high-κ ZrO_2 nanoparticles, in combination with CYELP, were used to generate high capacitance films for flexible OFET applications. By using solution processable high-κ ZrO_2 dielectrics and P3HT as the charge transport semiconductor layer, we have demonstrated flexible p-channel OFETs operated at V_{DS} of −2.0 V and V_{GS} in the range of 2.0 to −6.0 V, with a threshold voltage of −1.0 ± 0.2 V and a subthreshold swing of 0.3 V/dec. These flexible p-channel OFETs exhibited ON/OFF current ratios of $1.2 \pm 0.1 \times 10^3$ and average field effect hole mobility of 0.08 ± 0.012 cm^2/V·s. Currently, these high-κ ZrO_2 nanocomposites are being utilized for the generation of low operating voltage flexible floating gate memories using roll-to-roll (R2R) coating techniques.

AUTHOR INFORMATION

Corresponding Authors
*E-mail: abriseno@mail.pse.umass.edu (A.L.B.).
*E-mail: watkins@polysci.umass.edu (J.J.W.).

Author Contributions
†M.R.B. and J.K.B. contributed equally to this work.

Notes
The authors declare no competing financial interest.

REFERENCES

(1) Dimitrakopoulos, C. D.; Malenfant, P. R. L. *Adv. Mater.* **2002**, *14*, 99−117.
(2) Ponce Ortiz, R.; Facchetti, A.; Marks, T. J. *Chem. Rev.* **2010**, *110*, 205−239.
(3) Sun, J.; Zhang, B.; Katz, H. E. *Adv. Funct. Mater.* **2011**, *21*, 29−45.
(4) Dimitrakopoulos, C. D.; Mascaro, D. J. *IBM J. Res. Dev.* **2001**, *45*, 11−27.
(5) Majewski, L. A.; Schroeder, R.; Grell, M. *Adv. Mater.* **2005**, *17*, 192−196.
(6) Oh, J.-D.; Seo, H.-S.; Shin, E.-S.; Kim, D.-K.; Ha, Y.-G.; Choi, J.-H. *Appl. Phys. Lett.* **2013**, *103*, 063304.
(7) Lee, J.; Kim, J. H.; Im, S. *Appl. Phys. Lett.* **2003**, *83*, 2689.

13102

dx.doi.org/10.1021/am404129u | *ACS Appl. Mater. Interfaces* 2013, 5, 13096−13103

(8) Facchetti, A.; Yoon, M. H.; Marks, T. J. *Adv. Mater.* **2005**, *17*, 1705−1725.

(9) Veres, J.; Ogier, S.; Lloyd, G.; De Leeuw, D. *Chem. Mater.* **2004**, *16*, 4543−4555.

(10) Yoon, M.-H.; Yan, H.; Facchetti, A.; Marks, T. J. *J. Am. Chem. Soc.* **2005**, *127*, 10388−10395.

(11) Hwang, D. K.; Lee, K.; Kim, J. H.; Im, S.; Kim, C. S.; Baik, H. K.; Park, J. H.; Kim, E. *Appl. Phys. Lett.* **2006**, *88*, 243513.

(12) Yang, S. Y.; Kim, S. H.; Shin, K.; Jeon, H.; Park, C. E. *Appl. Phys. Lett.* **2006**, *88*, 173507.

(13) Jang, Y.; Kim, D. H.; Park, Y. D.; Cho, J. H.; Hwang, M.; Cho, K. *Appl. Phys. Lett.* **2006**, *88*, 072101.

(14) Kim, C.; Wang, Z.; Choi, H.-J.; Ha, Y.-G.; Facchetti, A.; Marks, T. J. *J. Am. Chem. Soc.* **2008**, *130*, 6867−6878.

(15) Cai, Q. J.; Gan, Y.; Chan-Park, M. B.; Yang, H. B.; Lu, Z. S.; Li, C. M.; Guo, J.; Dong, Z. L. *Chem. Mater.* **2009**, *21*, 3153−3161.

(16) Jung, C.; Maliakal, A.; Sidorenko, A.; Siegrist, T. *Appl. Phys. Lett.* **2007**, *90*, 062111.

(17) Chen, F.-C.; Chu, C.-W.; He, J.; Yang, Y.; Lin, J.-L. *Appl. Phys. Lett.* **2004**, *85*, 3295.

(18) Noh, H. Y.; Seol, Y. G.; Kim, S. L.; Lee, N.-E. *Electrochem. Solid State Lett.* **2008**, *11*, H218−H221.

(19) Maliakal, A.; Katz, H.; Cotts, P. M.; Subramoney, S.; Mirau, P. *J. Am. Chem. Soc.* **2005**, *127*, 14655−14662.

(20) Schroeder, R.; Majewski, L. A.; Grell, M. *Adv. Mater.* **2005**, *17*, 1535−1539.

(21) Huang, L.; Jia, Z.; Kymissis, I.; O'Brien, S. *Adv. Funct. Mater.* **2010**, *20*, 554−560.

(22) Yogo, T.; Yamamoto, T.; Sakamoto, W.; Hirano, S. *J. Mater. Res.* **2011**, *19*, 3290−3297.

(23) Guo, N.; DiBenedetto, S. a; Kwon, D.-K.; Wang, L.; Russell, M. T.; Lanagan, M. T.; Facchetti, A.; Marks, T. J. *J. Am. Chem. Soc.* **2007**, *129*, 766−7.

(24) Ramesh, G. V; Porel, S.; Radhakrishnan, T. P. *Chem. Soc. Rev.* **2009**, *38*, 2646−2656.

(25) Gur, I.; Fromer, N. A.; Geier, M. L.; Alivisatos, A. P. *Science* **2005**, *310*, 462−465.

(26) Lokhande, C. D.; Dubal, D. P.; Joo, O.-S. *Curr. Appl. Phys.* **2011**, *11*, 255−270.

(27) Hansen, J. A.; Wang, J.; Kawde, A.-N.; Xiang, Y.; Gothelf, K. V; Collins, G. *J. Am. Chem. Soc.* **2006**, *128*, 2228−2229.

(28) Wang, H.; Cui, L.-F.; Yang, Y.; Sanchez Casalongue, H.; Robinson, J. T.; Liang, Y.; Cui, Y.; Dai, H. *J. Am. Chem. Soc.* **2010**, *132*, 13978−13980.

(29) Park, Y. M.; Daniel, J.; Heeney, M.; Salleo, A. *Adv. Mater.* **2011**, *23*, 971−974.

(30) Xia, G.; Wang, S.; Zhao, X.; Zhou, L. *J. Mater. Chem. C* **2013**, *1*, 3291.

(31) Park, Y. M.; Desai, A.; Salleo, A.; Jimison, L. *Chem. Mater.* **2013**, *25*, 2571−2579.

(32) Wei, Q.; Tajima, K.; Hashimoto, K. *Appl. Phys. Lett.* **2010**, *96*, 243301.

(33) Wei, Q.; You, E.; Hendricks, N. R.; Briseno, A. L.; Watkins, J. J. *ACS Appl. Mater. Interfaces* **2012**, *4*, 2322−2324.

(34) Wei, Q.; Hashimoto, K.; Tajima, K. *ACS Appl. Mater. Interfaces* **2011**, *3*, 139−142.

(35) Onda, Y.; Muto, H.; Suzuki, H. Cyanoethylpullulan. U.S. Patent 4,322,524, March 30, 1982.

(36) Sayan, S.; Nguyen, N. V.; Ehrstein, J.; Emge, T.; Garfunkel, E.; Croft, M.; Zhao, X.; Vanderbilt, D.; Levin, I.; Gusev, E. P.; Kim, H.; McIntyre, P. *J. Appl. Phys. Lett.* **2005**, *86*, 152902.

(37) Hwang, D. K.; Lee, K.; Kim, J. H.; Im, S.; Park, J. H.; Kim, E. *Appl. Phys. Lett.* **2006**, *89*, 093507.

(38) Gu, G.; Kane, M. G.; Doty, J. E.; Firester, A. H. *Appl. Phys. Lett.* **2005**, *87*, 243512.

(39) Brown, A. R.; Jarrett, C. P.; De Leeuw, D. M.; Matters, M. *Synth. Met.* **1997**, *88*, 37−55.

(40) Koo, J. B.; Ku, C. H.; Lim, S. C.; Kim, S. H.; Lee, J. H. *Appl. Phys. Lett.* **2007**, *90*, 133503.

(41) Gu, G.; Kane, M. G.; Mau, S.-C. *J. Appl. Phys.* **2007**, *101*, 014504.

(42) Gu, G.; Kane, M. G. *Appl. Phys. Lett.* **2008**, *92*, 053305.

(43) Zschieschang, U.; Klauk, H.; Halik, M.; Schmid, G.; Dehm, C. *Adv. Mater.* **2003**, *15*, 1147−1151.

(44) Noh, Y. H.; Young Park, S.; Seo, S.-M.; Lee, H. H. *Org. Electron.* **2006**, *7*, 271−275.

(45) Lim, S. C.; Kim, S. H.; Koo, J. B.; Lee, J. H.; Ku, C. H.; Yang, Y. S.; Zyung, T. *Appl. Phys. Lett.* **2007**, *90*, 173512.

(46) Lee, S.; Koo, B.; Shin, J.; Lee, E.; Park, H.; Kim, H. *Appl. Phys. Lett.* **2006**, *88*, 162109.

(47) Egginger, M.; Irimia-Vladu, M.; Schwödiauer, R.; Tanda, A.; Frischauf, I.; Bauer, S.; Sariciftci, N. S. *Adv. Mater.* **2008**, *20*, 1018−1022.

(48) Xu, W.; Rhee, S.-W. *J. Mater. Chem.* **2009**, *19*, 5250.

(49) Xu, W.; Guo, C.; Rhee, S.-W. *J. Mater. Chem. C* **2013**, *1*, 3955−3960.

(50) Kim, S. H.; Yun, W. M.; Kwon, O.-K.; Hong, K.; Yang, C.; Choi, W.-S.; Park, C. E. *J. Phys. D: Appl. Phys.* **2010**, *43*, 465102.

(51) Chua, L.-L.; Zaumseil, J.; Chang, J.; Ou, E. C.-W.; Ho, P. K.-H.; Sirringhaus, H.; Friend, R. H. *Nature* **2005**, *434*, 194−199.

(52) McDowell, M.; Hill, I. G.; McDermott, J. E.; Bernasek, S. L.; Schwartz, J. *Appl. Phys. Lett.* **2006**, *88*, 073505.

(53) Briseno, A. L.; Mannsfeld, S. C. B.; Ling, M. M.; Liu, S.; Tseng, R. J.; Reese, C.; Roberts, M. E.; Yang, Y.; Wudl, F.; Bao, Z. *Nature* **2006**, *444*, 913−917.

(54) Briseno, A. L.; Tseng, R. J.; Ling, M.-M.; Falcao, E. H. L.; Yang, Y.; Wudl, F.; Bao, Z. *Adv. Mater.* **2006**, *18*, 2320−2324.

(55) Suo, Z.; Ma, E. Y.; Gleskova, H.; Wagner, S. *Appl. Phys. Lett.* **1999**, *74*, 1177.

(56) Gleskova, H.; Wagner, S.; Suo, Z. *Appl. Phys. Lett.* **1999**, *75*, 3011.

13103

dx.doi.org/10.1021/am404129u | *ACS Appl. Mater. Interfaces* 2013, 5, 13096−13103